ISIJ International, Vol. 64 (2024), No. 12, pp. 1847–1852
https://doi.org/10.2355/isijinternational.ISIJINT-2024-093

Short Article

Real-time Observation of Stress-strain Behavior beyond Necking in Martensitic Steel by *in-situ* Synchrotron X-ray Diffraction

Avala LAVAKUMAR,[1,2)*] Sukyoung HWANG,[1)] Kazuho OKADA,[3)] Myeong-heom PARK,[1)] Atul Haris CHOKSHI[4)] and Nobuhiro TSUJI[1)]

1) Department of Materials Science and Engineering, Kyoto University, Kyoto, 606-8501 Japan.
2) Department of Metallurgical and Materials Engineering, Indian Institute of Technology Ropar, Rupnagar, 140001 India.
3) Research Center for Structural Materials, National Institute for Materials Science (NIMS), 1-2-1 Sengen, Tsukuba, 305-0047 Japan.
4) Department of Materials Engineering, Indian Institute of Science, Bangalore, 560012 India.

(*Received March 30, 2024; Accepted August 13, 2024; Advance online published August 26, 2024; Published October 15, 2024*)

In general, the stress-strain relationship of materials obtained by standard uniaxial tensile test, which can identify the hardening behavior only up to necking. Beyond necking, the material behavior is usually estimated by extrapolating or numerical modelling based on hardening behavior prior to the uniform elongation. This study investigated the post-necking hardening behavior of a fully martensitic steel by *in-situ* synchrotron X-ray diffraction during tensile deformation. From the *in-situ* results, the dislocation density, lattice strain and phase stress were calculated within the necked region and outside the necked region. A near steady-state flow with some hardening was observed within the necked region of a martensitic steel. However, beyond uniform elongation, outside the necked region the dislocation density and phase stress decreased slightly, suggesting stress relaxation. Steady-state flow and dislocation densities at large strains suggest dynamic recovery occurs in the martensitic steel at room temperature.

KEY WORDS: martensitic steel; post-necking elongation; synchrotron radiation; tension test; plastic deformation.

1. Introduction

Metallic materials are often tested using uniaxial tensile tests to determine their flow properties such as the variation in stress with strain.[1)] A tensile stress-strain curve can be divided into two parts; from yielding up to ultimate tensile strength (UTS) where material deforms uniformly, and then from UTS to fracture where a material experiences flow localization. Such a variation in flow behavior has been well established for over a century, following Considère's criterion for uniform flow.[2)] While most conventional tensile testing is used to obtain the true stress-strain behavior up to the UTS, however, several metal forming operations such as press hardening and deep drawing may involve strains that exceed the uniform elongation of a material.[3)] Therefore, a knowledge of the post-necking stress-strain behavior of a material is essential to predict the forming ability and also crash events involving large strains under high-impact loads.

There has been a long desire to extend the applicability of tensile testing beyond uniform elongation, involving necking. Bridgeman[4)] conducted detailed studies in this regard and he proposed a method for determining the true stress-true strain behavior of cylindrical specimens beyond UTS. This correction involved the geometry of necking, with the curvature profile and diameter of the neck, and some analytical expressions. Later this concept was adapted by Aronofsky[5)] and others[6–8)] for flat sheet-type specimens having a rectangular cross-section geometry. In addition to a local area (neck profile) correction method, few other methods have been developed to determine the post-UTS stress-strain curves, including simple extrapolation methods[9)] and finite element based inverse methods.[10,11)] In extrapolation methods, power-hardening laws[12–15)] are typically used to describe the stress-strain relation in the pre-necked region, which is later extrapolated to the post-necked region. In the inverse method, the simulated result is compared with the experimental data by feeding the true stress-strain curve into the finite element program with intensive iterations. Thus, many researchers have considered the applicability of the uniaxial test in post-necking elongation region using a combination of the above analytical and simulation procedures, with associated complex assumptions. However, since the

* Corresponding author: E-mail: lava@iitrpr.ac.in

applied stress and corresponding strain have usually not been measured experimentally in the necked area, it is unclear that the resultant true stress-strain curves accurately represents material behavior beyond the UTS.

The purpose of this study is to simultaneously measure the stress and strain within a necked region and a region well away from the neck, to determine the true stress-strain behavior over the entire flow process until close to fracture. A fully martensitic steel was considered as a model material for this study, as it is widely used in modern car body structures, especially where high-impact loads are expected. Ishimoto *et al.*[16] investigated the deformation behavior in martensitic steel with a focus on block and packet structures, revealing that inhomogeneous deformation occurs during tensile testing. Koga *et al.*[17,18] used micro digital image correlation (DIC) to visualize strain distributions during tensile deformation in martensitic steel. They demonstrated that martensitic steel exhibits significant inhomogeneous deformability, which remains largely unchanged even in the late stages of necking deformation. Both studies highlighted the microscopic deformation mechanisms influencing crack nucleation and fracture behavior. In this study, we aim to reveal the macroscopic tensile behavior of lathe martensitic steel, including both the uniform and post-uniform deformation regions, to provide insights directly relevant to its mechanical performance. A combination of *in-situ* synchrotron X-ray diffraction (s-XRD) and DIC techniques were used to determine the stresses and strains within a diffuse necked region and outside of the neck part during tensile deformation, to understand the entire stress-strain curve of lathe martensitic steel.

2. Experimental Procedure

A low carbon steel with composition Fe-2.0Mn-0.1C (in wt.%) was selected for this study. The as received sheet was austenitized at 900°C for 1 hour and then cooled in the furnace to produce a ferrite + pearlite microstructure. After that the sheet was cold rolled to 90% thickness reduction, annealed at 820°C for 3 minutes in the single-phase austenite region and then quenched to room temperature to obtain fully martensite microstructure. For examining the microstructure, a specimen surface along the transverse direction was polished metallographically to obtain a mirror-like surface finish. Specimens were then electrochemically polished using 90%CH_3COOH + 10%$HClO_4$ solution at a voltage of 22 V for 30 seconds at room temperature. Microstructural observations were conducted utilizing a field-emission type scanning electron microscope (JSM7800F, JEOL), equipped with an electron back-scattering diffraction (EBSD) detector, which was operated at an acceleration voltage of 15 kV. The mechanical properties were calculated using uniaxial tensile test (AG-kN Xplus, Shimadzu) at room temperature with an initial strain rate of 8.3×10^{-4} s^{-1}. For tensile testing, specimens with dimensions (in mm) 10.0 (gauge length) × 2.5 (gauge width) × 1.0 (thickness) were machined from the heat-treated sheets. The displacement within the gauge section was sequentially captured with a CCD camera at five frames per second, and the resulting micrographs were processed with DIC software (Vic-2D 2009) to calculate the displacement or strain.

3. Results and Discussion

Figure 1(a) shows an SEM-EBSD orientation and grain boundary map of the 2Mn-0.1C steel, exhibiting a fully martensite microstructure consisting of a fine lath morphology. In the microstructure the high angle boundaries are highlighted in black, which represent the prior austenite grain boundaries, packet boundaries and block boundaries. Note that in lath martensite, according to the Kurdjumov-Sachs (K-S) relationship, the misorientation angle between the possible block boundaries is 10.53°. Therefore, a minimum misorientation angle of 10° is considered to highlight the boundaries.[19,20]

Figure 1(b) shows the engineering stress (s) - engineering strain (e) curve at room temperature of martensite steel, and Fig. 1(c) shows the corresponding true stress (σ) - true strain (ε) curve together with strain hardening rate (θ) curve. The true stress-strain curve is calculated by using relations $\sigma = s(1+e)$ and $\varepsilon = \ln(1+e)$. To address necking in our analysis, we applied the Considère criterion, a widely recognized method for identifying plastic instability and the onset of necking.[21] This criterion is based on the relationship between stress and strain, specifically where the strain-hardening rate ($d\sigma/d\varepsilon$) drops below the flow stress (σ) at given plastic strain rate ($\dot{\varepsilon}$):

$$\sigma \geq \left(d\sigma / d\varepsilon\right)\Big|_{\dot{\varepsilon}} \quad \text{..... (1)}$$

The martensitic steel shows a high yield strength (0.2% proof stress) and ultimate tensile strength around 1 060 MPa and 1 250 MPa, respectively. Since fine block boundaries are the most effective barriers to dislocation motion, they greatly contribute to an increase in the strength of the martensitic steel.[19] The data show limited uniform elongation of around 2.8%, and a relatively large amount of post-uniform elongation of around 7.4%. As usual, a higher strain hardening rate observed during the initial stage of deformation is followed by a hardening rate that decreased rapidly; the intersection of the true stress-strain curve with the θ-strain curve defines the onset of necking. The high strength with limited uniform elongation is a typical mechanical property of lath martensitic steels.[22–24]

Although the martensitic steel showed limited uniform elongation, the total nominal elongation reached up to 10%. Usually, due to a decrease in cross-sectional area, the tensile stress in necked region becomes higher than in un-necked region in a tensile specimen. As a result, however, the necked part is more strain-hardened than the un-necked region.[25] Thus, there is a considerable increase in the stress and strain/strain rate in the necked part of the gauge section, leading to local hardening. To understand this hardening behavior in the neck formation region *in-situ* synchrotron X-ray diffraction (s-XRD) experiments were performed at beamline BL46XU of SPring 8, Japan. **Figure 2**(a) shows a schematic illustration of the experimental setup and tensile specimen orientation. *In-situ* experiments were performed using the same dimensions as static tensile tests, except for the thickness of the specimen, which was around 0.5 mm for easy transmission of X-rays. For *in-situ* measurements, the X-ray energy was 30 keV (wavelength = 0.0413 nm), and the beam size was around 2 mm in the specimen width direction and 0.5 mm in the tensile direction. Prior to the

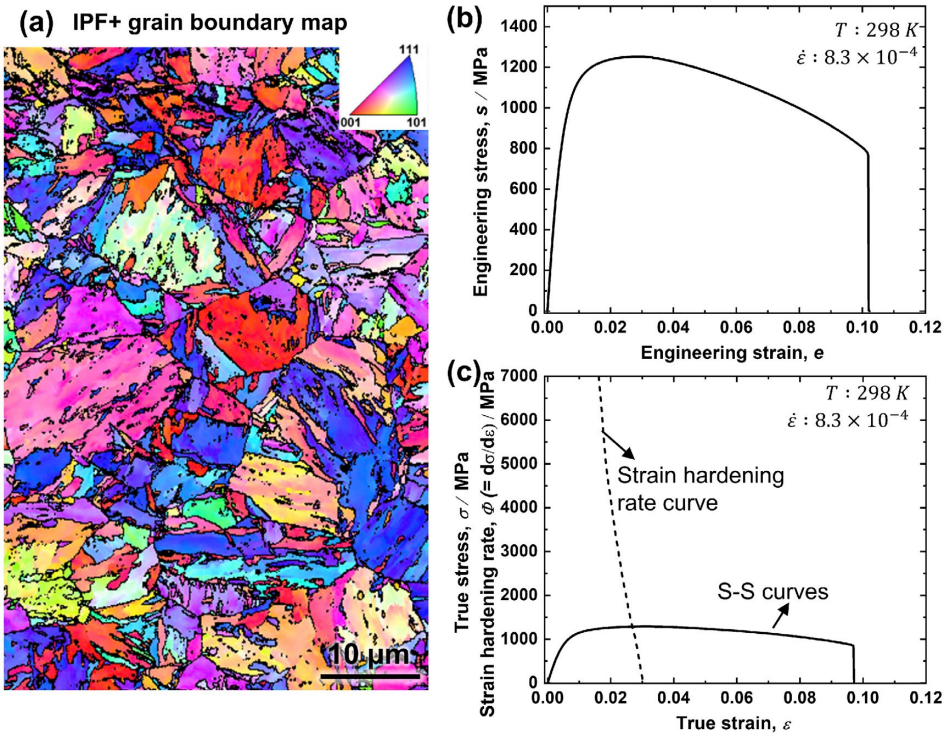

Fig. 1. Microstructure and mechanical characteristics of martensite (a) EBSD grain boundary + orientation colour map. Each colour in the orientation map represents a specific orientation according to the key stereographic triangle inserted in (a). (b) Engineering stress-strain curve and corresponding (c) True stress-strain curve together with strain hardening rate curve. (Online version in color.)

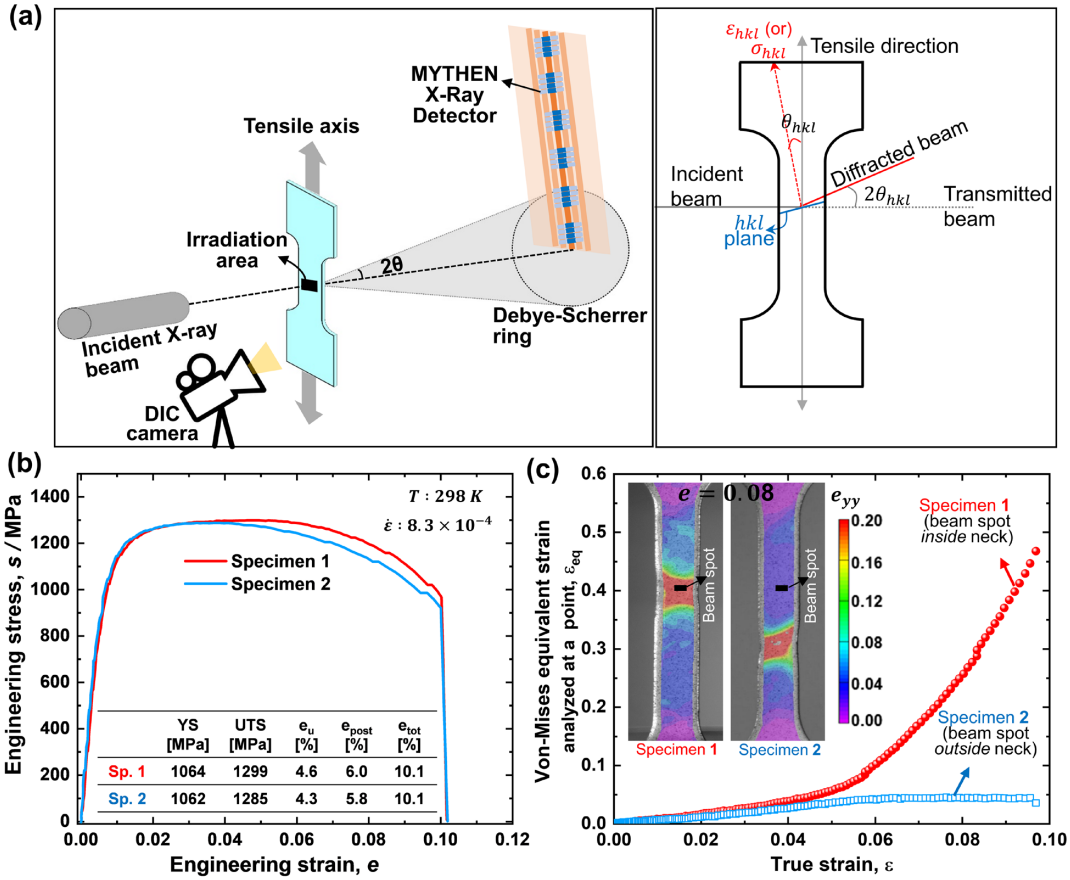

Fig. 2. (a) Schematic illustration of the experimental set-up of *In-situ* synchrotron X-ray diffraction with tensile test. Geometry of loading direction with respect to incident beam also shown in the right side. Note that the angle between the scattering vector and the tensile axis was very small. This is primarily due to short wavelength (0.0413 nm) of the X-ray beam utilized and the transmission geometry employed during the measurement. (b) Engineering stress-strain curve obtained from *in-situ* tensile tests and (c) Local strain at X-ray beam spot and strain distribution maps evaluated using DIC at a global strain of 0.08. (Online version in color.)

tensile test, a laser optical tuning was performed to ensure the exact beam position on the specimen. After precise alignment, tensile tests were performed at room temperature with an initial strain rate of 8.3×10^{-4} s^{-1} and XRD profiles were collected simultaneously at 1 second interval using serially connected six MYTHEN detectors (DECTRIS Ltd., Switzerland). Like static tensile tests, strain was also calculated precisely by a DIC method. Figure 2(b) shows the tensile stress-strain curves and mechanical properties of two representative martensitic steel specimens obtained during s-XRD experiments, depicting similar mechanical properties. During tensile deformation s-XRD profiles were acquired from the necked part in one specimen and in another specimen s-XRD profiles were acquired from outside of necked part. Hereafter these are referred to as inside neck and outside necked regions, respectively, instead of specimen 1 and specimen 2. Figure 2(c) shows the Von-Mises equivalent strain analysed inside and outside the necked region as a function of the true strain. The representative strain distribution maps of gauge portion of tensile specimen deformed to $\varepsilon=0.08$ are also shown in Fig. 2(c), where the X-ray beam spot positions are marked on both the specimens. Note that true strain is a valid measure up to the onset of necking. However, post-necking, true strain can become less reliable due to the development of complex multiaxial stress states. The Von-Mises equivalent strain, on the other hand, considers principal strains in different directions, that remains valid throughout the entire deformation process, including post-necking. Therefore, Von-Mises equivalent strain is chosen to compare both the necked and un-necked regions within a unified framework. In our study, the Von-Mises equivalent strain was calculated using the 2D-DIC software. It calculates accurate strain components (ε_{xx}, ε_{yy}, ε_{xy}) over the entire gauge length, including the necked region. These strain components are then used to calculate the Von-Mises equivalent strain (ε_{eq}), using the following formula:[17]

$$\varepsilon_{eq}=\frac{2}{3}\sqrt{\left[\left(\varepsilon_{xx}\right)^2+\left(\varepsilon_{yy}\right)^2-\varepsilon_{xx}\varepsilon_{yy}\right]} \quad \text{..... (2)}$$

As expected within the inside necked region the local strain was higher and increased up to 0.46, while the outside necked region strain value is around 0.045, which is about 10 times lower. These results suggest that once necking is initiated the plastic deformation continues to progress only within the necked region. Strictly speaking the necked region has a tri-axial stress state which is different from simple one outside the necked region. However, a recent study by Koga *et al.*[18] demonstrated that martensitic steel exhibits significant inhomogeneous deformability at a microscopic scale, with high-strain regions forming early and persisting through necking. They found that the deformation mode remained primarily uniaxial tension even in the late stages of necking. For consistency in our analysis, we focused on the uniaxial stress state to facilitate a comparative study of both conditions.

Figure 3 shows the dislocation density evolution corresponding to the inside and outside necked regions in selected specimens. The dislocation densities were evaluated from obtained s-XRD profiles by a convolutional multiple whole profile (CMWP) fitting method proposed by Ungár *et al.*[26–28] As mentioned previously, the obtained s-XRD profiles from specimen 1 and specimen 2 represents the characteristics within the necked region and outside the necked region, which closely represent the nature of deformation at post-uniform and uniform elongation region of martensitic steel. The value of the dislocation density before tensile deformation at both the locations matched closely at a high value of around $\sim3.3\times10^{15}$ m^{-2} due to the severely dislocated lath structure. During tensile deformation, the dislocation density is slightly increased to $\sim6.3\times10^{15}$ m^{-2} in the necked portion, while outside the necked region the dislocation density increases to $\sim5.3\times10^{15}$ m^{-2} and then decreased. It is interesting to note that the dislocation density remains essentially constant at large strains within the necked region.

To further understand the deformation behavior inside and outside the necked regions the orientation-specific lattice strain and stress evolution were examined. Lattice strain can be calculated by simply measuring the peak shift of diffraction profiles using the following equation.

$$\varepsilon_{hkl}=\frac{d_{hkl}-d^{o}_{hkl}}{d^{o}_{hkl}} \quad \text{..... (3)}$$

where ε_{hkl} is the lattice strain for the $\{hkl\}$ plane, and d^{o}_{hkl} and d_{hkl} are the interplanar spacings of $\{hkl\}$ planes in undeformed and deformed states, respectively. **Figure 4** shows the change in lattice strain of different $\{hkl\}$ planes as a function of Von-Mises equivalent strain (ε_{eq}) at inside (Fig. 4(a)) and outside neck region (Fig. 4(b)) of martensitic steel.

In composites deformed in iso-strain orientations, it is well known that the softer phase will transfer load to the harder phase. It is possible to consider such behavior even in anisotropic single-phase materials, where the different orientations have significantly different elastic moduli and strengths, such that weaker orientations yield first to transfer load to harder orientations.[29] For BCC martensite {110} is the stiffest orientation compared to {211} and {200} planes (Fig. 4). The {110} grains parallel to loading direction carry the highest load, to reach early yielding than the other grains; the {110} elastic lattice strain cease to increase after yield. As a result, {110} grains are expected

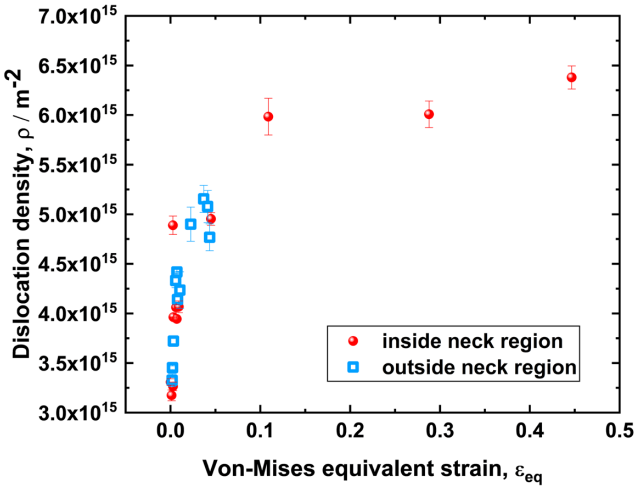

Fig. 3. Evolution of dislocation density inside and outside the necked region with reference to Von-Mises equivalent strain. (Online version in color.)

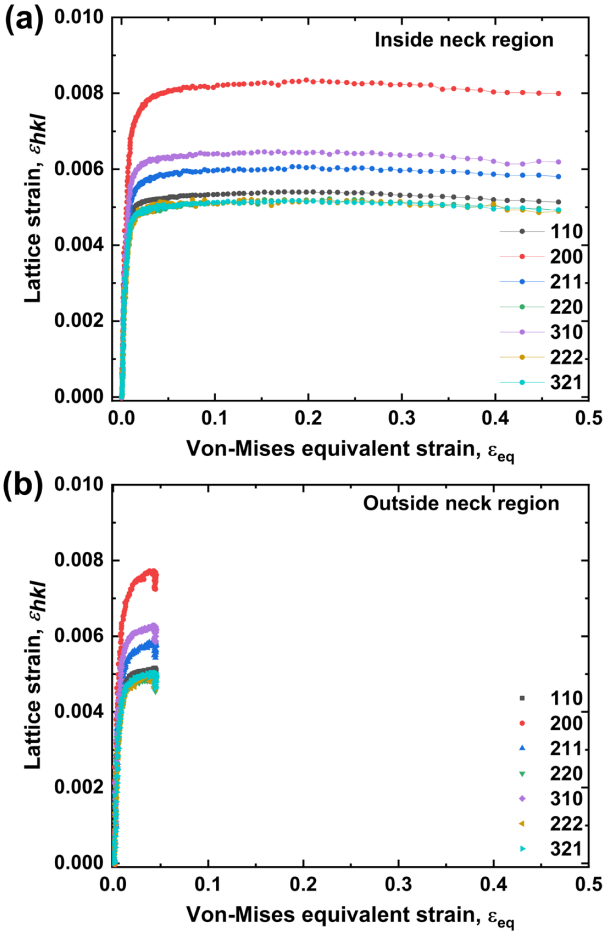

Fig. 4. Change in lattice strain of {*hkl*} planes against Von-Mises equivalent strain (ε_{eq}) (a) inside neck region (b) Outside neck region of martensitic steel. (Online version in color.)

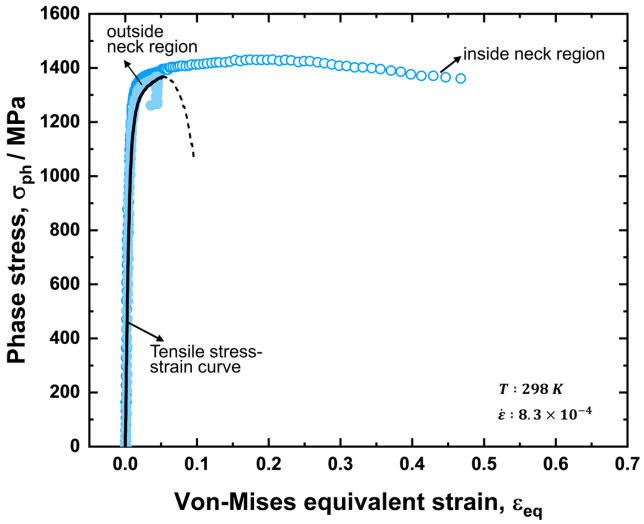

Fig. 5. Change in phase stress inside and outside the necked region with respect to Von-Mises equivalent strain. The true stress-strain tensile curve also plotted for comparison. In this figure the lattice stress of the {110} grain family is refrred to be the phase stress (σ_{ph}). (Online version in color.)

to transfer load to the more compliant orientations such as {200}, where large elastic strains will develop (Fig. 4). Overall, when the yielding occurred in each {*hkl*} plane, the lattice strains get partitioned so that the internal stresses get transferred from the orientations that are soft to those that are hard. When we compare orientation-specific lattice strains of these *hkl* planes at inside and outside neck, up to uniform elongation (~0.046), the lattice strains matched in both the cases (Fig. 4). However, the lattice strains within the necked region show a slight increase indicating small hardening in the necked part (Fig. 4(a)). For outside necked region the lattice strain value increased up to UTS and then decreased (Fig. 4(b)); coupled with the dislocation density decrease in Fig. 3. The data suggest stress relaxation outside the necked region, following the localization of flow within the necked region.

The elastic stress within each phase, known as phase stress, is determined using Hooke's law and considering Poisson's ratios based on phase strains. A common simplified approach assumes that phase strain corresponds to lattice strain along specific {*hkl*} planes, which is particularly useful when transverse strain data is unavailable for evaluating phase stress.[30,31] Since lattice strains measured are elastic, orientation-specific stresses can be calculated using a simplified form of Hooke's law:

$$\sigma_{hkl} = E_{hkl}\varepsilon_{hkl} \quad \text{..... (4)}$$

where σ, ε and E represent the stress, strain, and elastic modulus, respectively. For the stress calculation we have considered the {110} plane. The elastic modulus of {110} plane is calculated from the slope of the macroscopic stress versus lattice strain in the elastic regime. The calculated stress-strain curves from s-XRD are shown in **Fig. 5** together with the global tensile curve. It is noteworthy that while tensile testing shows an increase in strength up to the ultimate tensile strength (UTS) followed by a decrease. On the other hand, the phase stress versus Von-Mises equivalent strain data reveal steady-state flow up to large strains. Note that, the lattice stress of the {110} grain family is assumed to be the phase stress here. It can be seen that, the global tensile stress closely matches with the the σ_{110} phase stress (Fig. 5). In addition to the actual mix of orientations in the sample, a possible reason for this phenomenon could be due to geometry of the X-ray measurement. The lattice strains calculated from their lattice planes (*hkl*) perpendicular to the diffraction vector, which is also the direction of lattice strain ε_{hkl} (or σ_{hkl}) as shown in Fig. 2(a) (right). The lattice strains of the *hkl* planes are closely corresponded to the elastic strains observed in crystal family grains where the <*hkl*> directions align with the loading (tensile) direction. When diffraction angles were smaller (5.9°), such as in the {110} plane, this calculation was more accurate.[31] Besides, all the observed grain families including {110} showed steady-state behavior at larger strain (Fig. 4(a)). It seems martensite showed much potential of plasticity behavior in the necked part, which is consistent with the phase stress result showing steady-state behavior (Fig. 5). On the other hand, such a high (apparent) plasticity of martensite phase has also been reported in dual-phase steels with ferrite + martensite microstructure, where the local martensite strain is more than 40%.[32]

Although it is a hard phase, interestingly, in both single-phase and multi-phase steels, lath martensite shows high degree of ductility at strain localized regions. It is also interesting to note steady-state behavior at large strains

both in the dislocation density (Fig. 3) and lattice strains of different {*hkl*} planes (Fig. 4), which are similar to those of dynamic recovery in high-temperature deformation.[33] It is known that in BCC metals the cross-slip of screw dislocations is easier, and this enhances dynamic recovery, which might occurred in the current martensitic steel. Further, in case of lath martensite steel Du *et al.*[34] observed sliding of lath martensite substructure boundaries during micro-tensile deformation and Ohmura *et al.*[20] observed dislocation absorption at block boundaries by *in-situ* indentation in TEM, which could also contribute to recovery. Thus, it is reasonable to consider that dynamic recovery occurred during post-neck deformation and the enhanced recovery could reduce the stress concentration which initiates fracture, enabling large post-uniform elongation to failure.

4. Summary

In summary, a 2Mn-0.1C (wt.%) steel having a fully martensite microstructure showed relatively large post-necking elongation. *In-situ* synchrotron XRD measurements were carried out to understand the true stress-strain behavior in post-necking elongation region. From the *in-situ* results, the dislocation density, lattice strain and phase stress were calculated within the necked region and outside the necked region. It was observed that dislocation density is slightly increased initially and then remains essentially constant at large strains within the necked region. Further, lattice strain (or stress) also increased initially and a steady-state behavior was observed later. Steady-state flow and dislocation densities at large strains suggest dynamic recovery occurs in the martensitic steel at room temperature. However, beyond uniform elongation, outside the neck region the dislocation density and lattice strain values decreased suggesting that stress relaxation occurred.

Statement for Conflict of Interest

Authors declared that there are no conflicts of interest related to the conduct of this research.

Acknowledgments

This study was financially supported by JST CREST (JPMJCR1994), Elements Strategy Initiative for Structural Materials (ESISM, No. JPMXP0112101000), and KAKENHI (Grant-in-Aid for Scientific Research from the Japan Society for the Promotion of Science; No. 20K14608, 22K18888, 23H00234 and 23K13222), all through the Ministry of Education, Culture, Sports, Science and Technology (MEXT), Japan. All support is gratefully appreciated.

REFERENCES

1) N. Tsuji, S. Ogata, H. Inui, I. Tanaka, K. Kishida, S. Gao, W. Mao, Y. Bai, R. Zheng and J.-P. Du: *Scr. Mater.*, **181** (2020), 35. https://doi.org/10.1016/j.scriptamat.2020.02.001
2) S.D. Antolovich and R.W. Armstrong: *Prog. Mater. Sci.*, **59** (2014), 1. https://doi.org/10.1016/j.pmatsci.2013.06.001
3) V.C. Do, Q.-T. Pham and Y.-S. Kim: *Int. J. Adv. Manuf. Technol.*, **92** (2017), 4445. https://doi.org/10.1007/s00170-017-0441-8
4) P.W. Bridgman: *Trans. ASM.*, **32** (1944), 553.
5) B.J. Aronofsky: *J. Appl. Mech.*, **18(1)** (1951), 75. https://doi.org/10.1115/1.4010223
6) Z.L. Zhang, M. Hauge, J. Ødegård and C. Thaulow: *Int. J. Solids Struct.*, **36** (1999), 3497. https://doi.org/10.1016/S0020-7683(98)00153-X
7) E.E. Cabezas and D.J. Celentano: *Finite Elem. Anal. Des.*, **40** (2004), 555. https://doi.org/10.1016/S0168-874X(03)00096-9
8) I. Scheider, W. Brocks and A. Cornec: *J. Eng. Mater. Technol.*, **126(1)** (2004), 70. https://doi.org/10.1115/1.1633573
9) S. Coppieters, S. Cooreman, H. Sol, P. van Houtte and D. Debruyne: *J. Mater. Process. Technol.*, **211** (2011), 545. https://doi.org/10.1016/j.jmatprotec.2010.11.015
10) K.S. Zhano and Z.H. Li: *Eng. Fract. Mech.*, **49** (1994), 235. https://doi.org/10.1016/0013-7944(94)90006-X
11) P. Koc and B. Štok: *Comput. Mater. Sci.*, **31** (2004), 155. https://doi.org/10.1016/j.commatsci.2004.02.004
12) H. Hollomon: *Trans. AIME*, **162** (1945), 268.
13) Voce: *J. Inst. Met.*, **74** (1948), 537.
14) D.C. Ludwigson: *Metall. Trans.*, **2** (1971), 2825. https://doi.org/10.1007/BF02813258
15) A. Lavakumar, S.S. Sarangi, V. Chilla, D. Narsimhachary and R.K. Ray: *Mater. Sci. Eng. A*, **802** (2021), 140641. https://doi.org/10.1016/j.msea.2020.140641
16) Y. Ishimoto, M. Michiuchi, S. Nambu, K. Asakura, J. Inoue and T. Koseki: *J. Jpn. Inst. Metals*, **73** (2009), 720. https://doi.org/10.2320/jinstmet.73.720
17) N. Koga, M. Fujita, K. Shibata and S. Nanba: *ISIJ Int.*, **64** (2024), 491. https://doi.org/10.2355/isijinternational.ISIJINT-2023-121
18) N. Koga, M. Fujita and C. Watanabe: *Mater. Trans.*, **62** (2021), 1424. https://doi.org/10.2320/matertrans.MT-M2021118
19) C. Du, J.P.M. Hoefnagels, R. Vaes and M.G.D. Geers: *Scr. Mater.*, **116** (2016), 117. https://doi.org/10.1016/j.scriptamat.2016.01.043
20) J. Li, T. Ohmura and K. Tsuzaki: *Sci. China Ser. E*, **49** (2006), 10. https://doi.org/10.1007/s11431-004-5228-0
21) N. Tsuji, N. Kamikawa, R. Ueji, N. Takata, H. Koyama and D. Terada: *ISIJ Int.*, **48** (2008), 1114. https://doi.org/10.2355/isijinternational.48.1114
22) S. Harjo, T. Kawasaki, Y. Tomota, W. Gong, K. Aizawa, G. Tichy, Z. Shi and T. Ungár: *Metall. Mater. Trans. A*, **48** (2017), 4080. https://doi.org/10.1007/s11661-017-4172-0
23) T. Ungár, S. Harjo, T. Kawasaki, Y. Tomota, G. Ribárik and Z. Shi: *Metall. Mater. Trans. A*, **48** (2017), 159. https://doi.org/10.1007/s11661-016-3845-4
24) B. Hutchinson, P. Bate, D. Lindell, A. Malik, M. Barnett and P. Lynch: *Acta Mater.*, **152** (2018), 239. https://doi.org/10.1016/j.actamat.2018.04.039
25) H.W. Kim, S.B. Kang, N. Tsuji and Y. Minamino: *Acta Mater.*, **53** (2005), 1737. https://doi.org/10.1016/j.actamat.2004.12.022
26) T. Ungár, I. Dragomir, Á. Révész and A. Borbély: *J. Appl. Cryst.*, **32** (1999), 992. https://doi.org/10.1107/S0021889899009334
27) G. Ribárik and T. Ungár: *Mater. Sci. Eng. A*, **528** (2010), 112. https://doi.org/10.1016/j.msea.2010.08.059
28) G. Ribárik, J. Gubicza and T. Ungár: *Mater. Sci. Eng. A*, **387**–**389** (2004), 343. https://doi.org/10.1016/j.msea.2004.01.089
29) R. Purushottam Raj Purohit, A. Arya, G. Bojjawar, M. Pelerin, S. van Petegem, H. Proudhon, S. Mukherjee, C. Gerard, L. Signor, C. Mocuta, N. Casati, S. Suwas, A.H. Chokshi and L. Thilly: *Sci. Rep.*, **9** (2019), 79. https://doi.org/10.1038/s41598-018-36472-3
30) A. Lavakumar, M.H. Park, S. Hwang, H. Adachi, M. Sato, R.K. Ray, M. Murayama and N. Tsuji: *Mater. Sci. Eng. A*, **874** (2023), 145089. https://doi.org/10.1016/j.msea.2023.145089
31) S. Gao, T. Yoshimura, W. Mao, Y. Bai, W. Gong, M.H. Park, A. Shibata, H. Adachi, M. Sato and N. Tsuji: *Crystals*, **10(12)** (2020), 1115. https://doi.org/10.3390/cryst10121115
32) H. Ghadbeigi, C. Pinna, S. Celotto and J.R. Yates: *Mater. Sci. Eng. A*, **527** (2010), 5026. https://doi.org/10.1016/j.msea.2010.04.052
33) R.R. Eleti, T. Bhattacharjee, A. Shibata and N. Tsuji: *Acta Mater.*, **171** (2019), 132. https://doi.org/10.1016/j.actamat.2019.04.018
34) C. Du, R. Petrov, M.G.D. Geers and J.P.M. Hoefnagels: *Mater. Des.*, **172** (2019), 107646. https://doi.org/10.1016/j.matdes.2019.107646